Irregular Layout for a Satellite's Interferometric Array

Paul Krzakala, Amine Assouel, Max Dunitz, Eric Anterrieu, *Member, IEEE*, François Cabot, Ali Khazaal, Nemesio Rodriguez-Fernandez, Bernard Rougé, Jean-Michel Morel, Yann H. Kerr, *Member, IEEE*, and Miguel Colom

***Abstract*—We address the optimization problem of antenna placement on satellite-mounted interferometric synthetic-aperture instruments. In classic designs, the antennas on satellites are aligned regularly on the satellite's frame. Inspired by methods proposed for the placement of antennas in astronomical interferometers, such as ALMA or SKA, we explore irregular layouts and show that they are a valid alternative in terms of spatial resolution and reconstruction error. We formalize mathematically the optimization problem of irregularly placed antennas and we show that this kind of arrays can still be calibrated with the same methods used for regular arrays. Finally, this strategy is evaluated in the context of soil moisture and ocean salinity (SMOS) follow-up concepts, such as SMOS-HR (high resolution), for which the new optimized irregular configurations are compared to the regular ones.**

***Index Terms*—Antenna arrays, differentiation (mathematics), Fourier transforms, optimization methods, radio interferometry.**

I. Introduction

THE retrieval of accurate brightness temperature maps of the Earth from space is imperative for the production of reliable estimates of soil moisture and ocean salinity (SMOS) and two essential climate variables (ECVs) [1]. Recovering such brightness temperature maps from spaceborne radiometric measurements is a key component of the SMOS satellite mission [2]. SMOS was launched in 2009 and is still operational, though operating well beyond its nominal expected mission lifetime of three years. The SMOS instrument consists of $N = 69$ LICEF antennas spaced by $R = 0.87\lambda$ m operating within the protected L-band ($\lambda \approx 0.21$ m).

The L-band has been extensively used in radio astronomy and Earth-observation satellites, such as SMOS [2]–[4], since it is not heavily attenuated by the atmospheric constituents and not strongly perturbed by the ionosphere. In addition, L-band radiation is less affected by the vegetation than higher frequencies, allowing accurate estimation of surface variables such as soil moisture.

The SMOS instrument receives the radiation emitted from the Earth's surface, which can then be related to the moisture content in the first few centimeters of soil over land, and to salinity in the surface waters of the oceans [2].

With SMOS still operating after more than twice its expected lifetime, new designs for a follow-on mission are under study. SMOS-HR (high resolution) is currently under study by the *Centre National d'Etudes Spatiales* [5]–[7]. As SMOS, the SMOS-HR is an aperture synthesis radiometer, but with baselines up to 17 m to provide a spatial resolution up to 10 km, three times better than that of the SMOS.

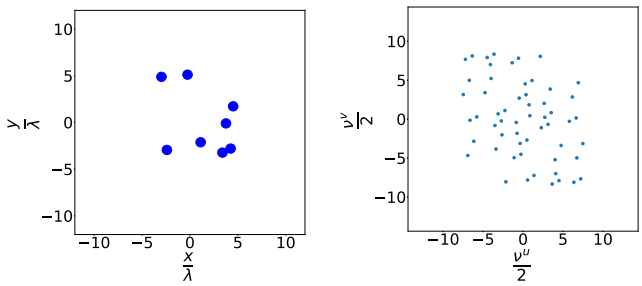

Fig. 1. Random spatial layout of antennas on the left and associated layout of baselines on the right with $N = 8$ antennas. The sampling frequencies are obtained from the baselines, the vectors joining each possible pair of antennas.

A. Positioning the Problem

In this study, we focus on how to place the antennas of the synthetic aperture instrument (an array of antennas) in order to obtain a brightness temperature map of low error that also maximizes the alias-free field of view (FOV).

Fig. 1 shows the baselines associated to an interferometer whose antennas are randomly placed on a plane: To each pair of antennas *(i,j)*, respectively, placed at $a_i = (x_i, y_i)$ and $a_j = (x_j, y_j)$ on the satellite's planar frame, is associated a baseline vector $\nu_{i,j} = \frac{a_i - a_j}{\lambda}$, where λ is the wavelength of the signal received by the interferometer. We denote by $\nu^u_{i,j}$ and $\nu^v_{i,j}$ the two components of the vector in the $u - v$ frequency plane.

Manuscript received May 30, 2021; revised August 6, 2021; accepted August 21, 2021. Date of publication September 2, 2021; date of current version September 30, 2021. *(Corresponding author: Miguel Colom.)*

Paul Krzakala, Amine Assouel, Max Dunitz, Jean-Michel Morel, and Miguel Colom are with the Department of Mathematics, Paris-Saclay Normal School, Gif-sur-Yvette 91190, France (e-mail: paul.krzakala@ens-paris-saclay.fr; amine.assouel@ens-paris-saclay.fr; max.dunitz@ens-paris-saclay.fr; jean-michel.morel@ens-paris-saclay.fr; miguel.colom-barco@ens-paris-saclay.fr).

Eric Anterrieu, François Cabot, Ali Khazaal, Nemesio Rodriguez-Fernandez, Bernard Rougé, and Yann H. Kerr are with CNES, Centre d'Etudes Spatiales de la Biosphere, Toulouse 31400, France (e-mail: eric.anterrieu@cesbio.cnes.fr; Francois.Cabot@cesbio.cnes.fr; ali.khazaal@cesbio.cnes.fr; nemesio.rodriguez@cesbio.cnes.fr; bernard.rouge@cesbio.cnes.fr; yann.kerr@cesbio.cnes.fr).

Digital Object Identifier 10.1109/JSTARS.2021.3109730

By the Van Cittert–Zernike theorem [8], correlating the signal of both antennas leads to the measurement of a visibility function defined for each couple of antennas (i,j) by

$$V_{i,j}(u,v) = \int_{\left\|\binom{\xi}{\eta}\right\|_2<1} \frac{F_{i,j}[\xi,\eta]}{\sqrt{1-\xi^2-\eta^2}} T[\xi,\eta] e^{-2i\pi(\nu^u_{i,j}\xi+\nu^v_{i,j}\eta)} d\eta d\xi \quad (1)$$

where $F_{i,j} = F_i \times \overline{F_j}$ is the product of the antenna radiation pattern (ARP) functions of antennas i and j, η and ξ are the direction cosines with respect to the axes of the $u-v$ plane. In our experiments, we will assume that any antenna can be modeled as radial function $F_i = \pi^2 \cos^2(\theta)$, with $\theta = \text{asin}(\sqrt{\xi^2+\eta^2})$.

In the following, we will write $\widetilde{T}[\xi,\eta] = T[\xi,\eta] \times \frac{F_{i,j}[\xi,\eta]}{\sqrt{1-\xi^2-\eta^2}}$ (the *modified* brightness temperature) to lighten the notation, with

$$\frac{F_{i,j}[\xi,\eta]}{\sqrt{1-\xi^2-\eta^2}} = \begin{cases} \pi^4(1-\xi^2-\eta^2)^{\frac{3}{2}} & \text{if } ||(\xi,\eta)||_2 < 1 \\ 0 & \text{otherwise} \end{cases}.$$

The visibilities, therefore, can be written as

$$V = \boldsymbol{\mathcal{F}}\left\{\widetilde{T}\right\} + \boldsymbol{\mathcal{N}}(0,\sigma_i) \quad (2)$$

where $\boldsymbol{\mathcal{N}}(0,\sigma_{N_i})$ is zero-mean white Gaussian noise with standard deviation σ_i added to visibility i, for $1 \le i \le N$, and $\boldsymbol{\mathcal{F}}\{.\}$ is the Fourier transform operator. The noise level for the SMOS radiometer is well-known [9]; its standard deviation is

$$\sigma_i = V_{\text{dc}}/\sqrt{m_i 2B\tau} \quad (3)$$

where V_{dc} is the dc component of $\boldsymbol{\mathcal{F}}\{\widetilde{T}\}$, m_i is the multiplicity of baseline i, B is the bandwidth, and τ is the integration time. Thus, each baseline $b_{i,j}$ is associated with a sample $V_{i,j}[u,v] = V_{\nu_{i,j}}(u,v)$ of the Fourier transform of the *modified* temperature $\widetilde{T}$. To recover a large-FOV and low-error temperature map, the chosen antenna array design must ensure that the baselines provide a proper (dense, uniform, without "holes") coverage of the $u-v$ plane.

The optimization of an irregular layout of antennas is a well-known problem [10]–[12]. However, satellite deployment imposes additional constraints on the layout (such as strict limits on the size, weight, and mechanical complexity of the instrument, which can make the problem of avoiding overlapping antennas nontrivial, as well as the requirement of sufficient redundancy in the baselines to allow for self-calibration), and optimal antenna layouts found using traditional approaches may not be feasible in this context. Because of these tight constraints, regular placement of the antennas along simple geometric frames, such as polygons, as illustrated in Fig. 2, is a natural choice as it greatly reduces the complexity of the problem. This approach was used for SMOS [13], and is also considered for its successors [7]. The well-known drawbacks of this choice are the inevitable redundancy of some baselines (see Fig. 2), which prevent adequate sampling of the Fourier domain and thus spatial folding, as illustrated in Fig. 19.

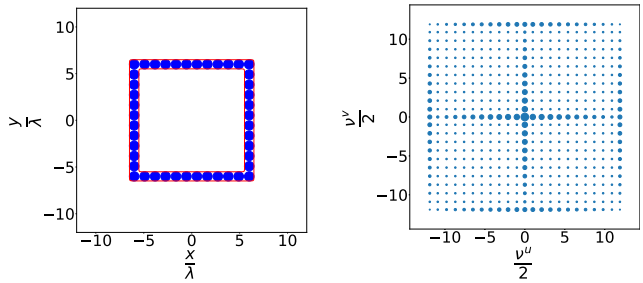

Fig. 2. Uniform layout of antennas on a square satellite frame (left) and its baselines (right) with $N = 44$ antennas. Each dot represents a baseline and its size is proportional to its multiplicity. A uniform layout induces many redundancies due to the symmetries involved. In this configuration, each baseline has a multiplicity $m \ge 2$ and the baselines $(1,0)$, $(-1,0)$, $(0,1)$, and $(0,-1)$ each has multiplicity 22. Here the antennas—and their weight—are being used inefficiently, redundantly sampling certain baselines and, as a result, undersampling the $u-v$ plane, which can produce spatial folding in the reconstruction of brightness temperatures from the visibilities.

Inspired by the methods used for optimizing the placement of radio telescopes in Earth-based astronomical interferometers, such as ALMA and SKA [14], [15], such as the method developed in [16], we consider the problem of choosing irregular layouts for a spaceborne interferometer, such as the SMOS successor, and propose a new algorithm for optimizing the antenna placement in this context. In the next section, we describe how the state-of-the-art has addressed these questions in different contexts.

B. An Overview of Optimization Methods

The antenna array optimization problem can be traced back to a first paper published in 1968 by T. Moffet investigating "minimum-redundancy linear arrays" [10]. While different inteferometer array shapes have long been in use [17], the antenna array optimization problem on these shapes is more recent [11].

Current approaches use heuristics to express multiple spatial constraints. For instance, Oliveri *et al.* [18] minimizes a cost function of the form $\frac{1}{B}$, where B is the number of cells in the $u-v$ plane (gridded uniformly) that are sampled for each given layout. Such a cost function is not differentiable, and is therefore minimized by using a combination of a genetic algorithm and the almost different sets (ADS) method. A similar method is developed in [14], where a particle swarm optimization (PSO) algorithm is used to search for optimal layouts.

In the pressure forces method [16] by Boone, each of the N antennas moves through actions on its associated N Fourier associated samples. A pressure force is applied to the baselines to push them away from the areas where the density of baselines exceeds a target density in the $u-v$ plane. Each antenna, therefore, moves according to the sum of the pressure forces applied to the N baselines it is involved in. This optimization principle is illustrated in Fig. 3 . Fig. 4. shows the pressure forces associated with the configuration in Fig. 1.

In 2004, Y. Su *et al.* proposed a novel "sieving" algorithm, which starts with a very large number of antennas and gradually removes the less useful elements until it reaches a suitable configuration [19].

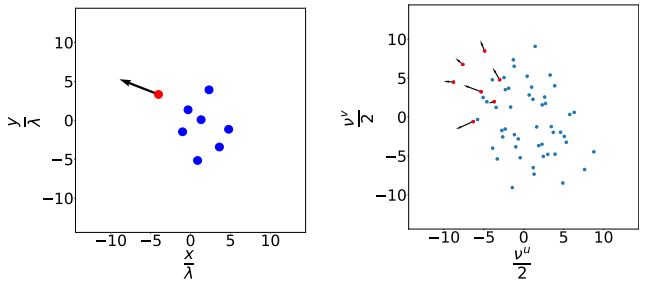

Fig. 3. Pressure force on the red antenna on the left, resulting from the pressure forces on its associated red baselines on the right.

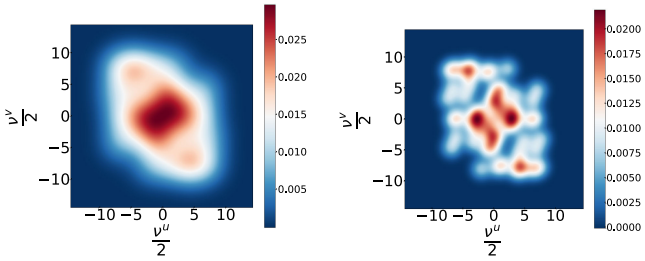

Fig. 4. Densities associated with the random layout of Fig. 1 for $\sigma_1 = \sigma_0$ and $\sigma_2 = \frac{\sigma_0}{2}$ on the left and right, respectively. Here $\sigma_0 = \sqrt{\frac{S}{|B|}}$, S is the surface on which one can place the baselines and $|B|$ the number of baselines.

Another independent approach is suggested in [20], where the u, v samples are projected onto a one-dimensional vector. An equivalent projection is done for an ideal model distribution, and the difference between these vectors yields correction terms, which can be mapped to new antenna positions. Such modifications are iterated in all directions until a close match is achieved to the desired u, v plane coverage.

To summarize, a variety of specific methods have been designed to solve the configuration problem, yet no consensus has emerged. In the current article, we show that instead of designing a specific method to solve the configuration problem, it can be reduced to the classical minimization of a differentiable functional by the careful design of an appropriated cost function. The optimization of the aforementioned functional can then be performed with the classical gradient-based tools, whose scalability has significantly improved recently as a consequence of the rapid development of machine learning. Indeed, this quick development has led to the refinement of methods (automatic differentiation) and hardware (GPU) that plays a great role in the approach we develop.

The rest of this article is organized as follows. Section II defines the minimization problem, which is reduced to a cost function for which we detail the parameters. Section III addresses the problem of minimizing the cost function defined in Section II, as well as discussing how to discretize the problem choosing a Lagrangian-like approach to solve the constrained problem and picking the right hyperparameters. Section IV presents the specific issues raised in the context of a satellite, namely the need for a configuration that can be actually calibrated, and the minimal distance between antennas to avoid overlapping. We discuss potential successors of SMOS as an application of our approach. In Section V, we present our results and evaluate them with two SMOS-HR candidates. In particular, we use simple theoretical arguments to develop a visual representation of the quality of a layout. In particular, we associate a kernel representing the impulse response of the instrument to each antenna configuration. We show simulated experimental results for the brightness temperature maps using two different scenes. We use them to compare the results of our irregular layouts with those obtained with two regular ones, the square and cross quincunxes, which have been considered for the SMOS-HR. Finally, Section VI concludes the article.

II. The Minimization Problem

Given a set $A = \{a_i\}, i \in [1, \dots, N]$ containing the position of N antennas on a plane, we consider the set $B = \{a_i - a_j\}, a_i, a_j \in A$ of its associated baselines. Denoting by $\mathbb{S}_\mathbb{A} \subset \boldsymbol{\mathcal{R}}^2$ the planar region constraining the antennas, it follows that the baselines $b \in B$ belong to $\mathbb{S}_\mathbb{B} = \mathbb{S}_\mathbb{A} - \mathbb{S}_\mathbb{A}$. Our goal is then to optimize the positions of the antennas $a_i \in \mathbb{S}_\mathbb{A}$ so that $\mathbb{S}_\mathbb{B}$ is well sampled by the baselines b_{ij}. This requires a quantification of the sampling quality, which relies on the computation of a baseline density function $\mathbf{d_B}$ and its comparison with an ideal/target density $\mathbf{d_t}$. As developed in [21], the choice of $\mathbf{d_t}$ entirely relies on the scientific purposes of the interferometric array, the typical choice being a Gaussian or an uniform density $\mathbf{d_t} = \frac{1}{|\mathbb{S}_\mathbb{B}|}\mathbb{1}_{\mathbb{S}_\mathbb{B}}$, where $|.|$ is the area.

To compute $\mathbf{d_B}$, we consider the following two ways:

- either by computing the number of baselines in the vicinity of each point, which depends on a scale parameter ϵ, so that

$$\mathbf{d}^\epsilon_\mathbf{B}(u) = \frac{\text{card}(D(u,\epsilon) \cap B)}{\pi\epsilon^2} \tag{4}$$

  where $D(u, \epsilon)$ is the circle of center u and radius ϵ and card(.) the cardinality; and
- or by convolving the Dirac baseline comb with a Gaussian kernel, which requires a scale parameter σ, so that

$$\mathbf{d}^\sigma_\mathbf{B}(u) = \left(\sum_{b\in B} \delta_b * g_\sigma\right)(u) = \frac{1}{2\pi\sigma^2}\sum_{b\in B} e^{-\frac{|b-u|^2}{2\sigma^2}} \tag{5}$$

  where δ_b is the Dirac mass at b and g_σ the Gaussian of variance σ^2. Fig. 5 shows an example of the computation of the density with (5).

Both (4) and (5) for $\mathbf{d_B}$ can be seen as a convolution and are characterised by a parameter representing a typical distance or scale. Equation (5) is preferred for optimization because it is differentiable and there exist efficient optimization algorithms in that case. Following the above considerations, we define our cost function as

$$C(A, \sigma) = \int_{\mathbb{S}_\mathbb{B}} f(\mathbf{d_B}(u, \sigma) - \mathbf{d_t}(u))du \tag{6}$$

where A is the unknown antenna layout and f a distance function to the target density. The question now is how to specify f, σ, and $\mathbf{d_B}$. In the following, we explain how.

We address first the choice of $\mathbf{d_B}$. We opt for the second formula with a Gaussian, since it has the advantage of being

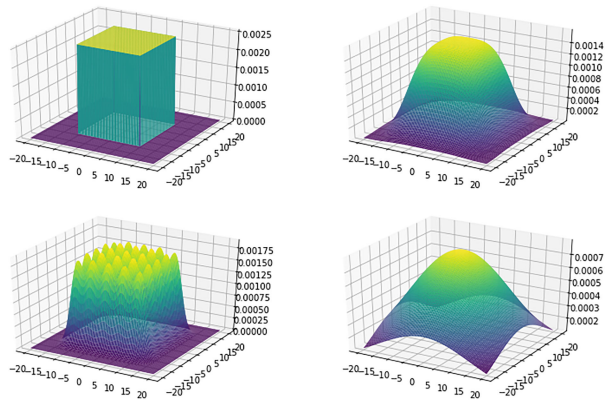

Fig. 5. Classic formulation of the problem where a uniform coverage of the $u-v$ plane is sought for. The target density $\mathbf{d_t}$ is uniform and the ideal layout of the baselines B_i is a regular grid. Top left: the target density. Top right: $\mathbf{d}^{\sigma}_{\mathbf{B_i}}$ with $\sigma = \sigma_0$. Note that this ideal density, associated with the ideal layout of the baselines B_i, is close to the target density. Therefore, minimizing the distance (6) to the target density implies being close to the ideal layout of the baselines: the cost function represents properly the problem. Bottom left: $\mathbf{d}^{\sigma}_{\mathbf{B_i}}$ with $\sigma = 0.5\sigma_0$. With such a standard deviation, a sum of Gaussians cannot approximate a uniform distribution. Bottom right: $\mathbf{d}^{\sigma}_{\mathbf{B_i}}$, the same problem with $\sigma = 2\sigma_0$.

differentiable. Still, we must fix σ so that the induced cost function is adapted to the problem. We shall denote by $\mathbf{B}_I$ an "Ideal" set of baselines, i.e., a set of baselines that is perfectly suited to the scientific application but not necessarily attainable with a feasible antenna layout. Given that we aim for a uniform coverage of the $u-v$ plane, $\mathbf{B}_I$ is, therefore, on a uniform grid. Because $\mathbf{B}_I$ is such an ideal set of baselines, the cost function should be as low as possible when evaluated in $\mathbf{B}_I$. This leads us to define σ as the solution of the convex minimization problem (7). This problem is illustrated in Fig. 5.

$$\sigma_1 = \arg\min_{\sigma>0} \int_{\mathbb{S}_\mathbb{B}} f(\mathbf{d}^{\sigma}_{\mathbf{B_I}}(u) - \mathbf{d_t}(u))du = \arg\min_{\sigma>0} C(\sigma). \tag{7}$$

A simpler approach could have been to define a scale parameter σ that is compatible with the typical surface of the problem, namely $\sigma_0^2 = \frac{|\mathbb{S}_\mathbb{B}|}{|B|}$. This heuristic σ_0 is actually used as an initialization for the minimization by gradient descent of (7). Fig. 6 shows the landscape of the convex minimization problem (7), which confirms that σ_0 is a good initialization for the gradient descent.

We now address the question of an adequate form for the function f. For an accurate image reconstruction, what matters is to avoid holes in the coverage. In the contrary, a higher density than the target density simply implies a richness of sampled baselines in the region, which cannot on its own reduce the quality of the resulting brightness temperature image. Consequently, we designed functions f that only increase the cost when $\mathbf{d_B} < \mathbf{d_t}$. We, therefore, consider $\{f_\alpha/\alpha \in \mathbb{N}^*\}$, where α is an hyperparameter usually set to 2 and

$$f_\alpha(x) = \begin{cases} 0 & \text{if } x > 0 \\ |x|^\alpha & \text{otherwise} \end{cases}.$$

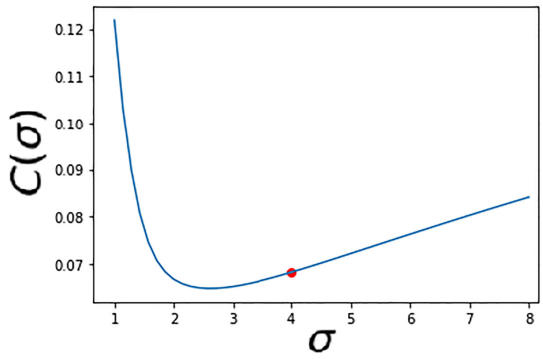

Fig. 6. Plot of the cost function $\sigma \to C(\sigma)$ for problem (6) and 40 antennas. The red dot represents the value $\sigma_0^2 = \frac{|\mathbb{S}_\mathbb{B}|}{|B|}$, which is a good initialization to start approaching the minimum.

When $x > 0$, there is a higher density than the target, and when $x < 0$, there is a deficit. In practice, the values of $\mathbf{d_B}$ and $\mathbf{d_t}$, though never identical, are always close, and the value of $\frac{\mathbf{d_B}}{\mathbf{d_t}}$ generally stays between $\frac{1}{2}$ and 2. Thus, we decided to normalize the cost function so that the value taken by the cost becomes easy to interpret, as

$$C(A,\sigma) = \left(\frac{1}{|\mathbb{S}_\mathbb{B}|} \int_{\mathbb{S}_\mathbb{B}} f_\alpha \left(\frac{\mathbf{d_B}(u,\sigma)}{\mathbf{d_t}(u)} - 1 \right) du \right)^{1/\alpha}. \tag{8}$$

The majority of values of C are between 0 and 1 with this formulation.

III. Discrete Formulation and Optimization

The whole layout will be optimized by moving all the antennas of the instrument at each iteration of the optimization process. The reason behind this choice is that, given a number of antennas (on the order of $N \simeq 200$), an optimization antenna by antenna may get stuck in a local minimum. Indeed, moving only one antenna leads to the displacement of $N-1$ baselines, and therefore, the whole configuration is changed, making it less likely to stop in local mimima. We observed that a classic constrained gradient descent works. The geometric constraints imposed by the shape of the satellite (see Section IV-C) are smooth enough, so that there is no *Swiss cheese effect*; that is, the constrained domain $\mathbb{S}_\mathbb{A}$ is not plagued with holes that would make constrained gradient descent ineffective.

In order to compute the cost function (7), we will use a discrete version of (7) by associating a grid Gr with $\mathbb{S}_\mathbb{B}$. The minimization problem (7) becomes

$$\left(\frac{1}{|S_B|} \sum_{b \in Gr} f_\alpha \left(\frac{\mathbf{d_B}}{\mathbf{d_t}}(b) - 1 \right) \right)^{1/\alpha}. \tag{9}$$

An adequate choice of the grid Gr is a key ingredient to the success of the method. To keep the algorithm as simple and natural as possible, we opted for a uniform grid

$$G_\delta = \{\delta k \;\; k \in \mathbb{Z}^2 \} \cap |\mathbb{S}_\mathbb{B}|.$$

The value of δ is the result of a compromise between accuracy and complexity. It must be small enough to detect gaps in the

Algorithm 1: Antennas To Baselines($\mathbf{A}$).

Input: $\mathbf{A} \in M_{2,n}(\mathbf{R})$ where n is the number of antennas and $A_{1,i} = a_i^x$, $A_{2,i} = a_i^y$ the coordinates of antenna #i.
Output: $\mathbf{B}$, the baselines associated with $\mathbf{A}$.
$\mathbf{A}_n \leftarrow \mathbf{A}$.`Repeat(n)` {Creates a $2 \times n \times n$ tensor by stacking n times $\mathbf{A}$}
$\mathbf{B} \leftarrow \mathbf{A}_n -$ Transpose($\mathbf{A}_n$)
$\mathbf{B}_{k,i,j} \leftarrow A_{k,i} - A_{k,j} = (b_{i,j})_k$
$\mathbf{B} \leftarrow \mathbf{B}$.Reshape($2\ N^2$)
return B

Algorithm 2: Compute Local Density($\mathbf{B}$,U, σ).

Input: **B** the baselines,
U: point on which we want to compute the density
σ: kernel parameter discussed above.
$D \leftarrow (\mathbf{B} - U_x)[0]^2 + (\mathbf{B} - U_y)[1]^2$
Output: the local density matrix.
$\mathbf{G} \leftarrow \frac{1}{2\pi\sigma^2} \exp(-\frac{D}{2\sigma^2})$
return $\mathbf{G}$.$Mean()$

Algorithm 3: Cost Function($\mathbf{A}$,$\mathbf{G}_r$,α, f_α,d_t).

Input: $\mathbf{A} \in M_{2,n}(\mathbf{R})$ where n is the number of antennas and $A_{1,i} = a_i^x$, $A_{2,i} = a_i^y$ the coordinates of antenna #i.
$\mathbf{G}$: The grid
σ: Kernel parameter
α: Constraint parameter
f_α: The constraint function
d_t: The target density function
Output: the cost associated to the given array of antennas.
$\mathbf{B} \leftarrow$ AntennasToBaselines($\mathbf{A}$)
$\mathrm{C} \leftarrow 0$
for $u \in G$ **do**
  $D \leftarrow$ ComputeLocalDensity($\mathbf{B}, U, \sigma$)
  $C \leftarrow C + f_\alpha(\frac{D}{d_t(u)-1})$
end for
return $(\frac{1}{|\mathbb{S}_\mathbb{B}|}\mathrm{C})^{1/\alpha}$

coverage of $\mathbb{S}_\mathbb{B}$ by the baselines. If the baselines were uniformly distributed, the typical surface occupied by a baseline would be $\frac{|\mathbb{S}_\mathbb{B}|}{|B|}$. Thus, we define a frequency gap as a round area of size $2\frac{|\mathbb{S}_\mathbb{B}|}{|B|}$ containing no baseline. Detecting such gaps leads to impose a maximal value on δ

$$\delta^2 < 2\frac{|\mathbb{S}_\mathbb{B}|}{|B|}. \tag{10}$$

Thus, we must have $\delta = \lambda\delta_0$, where $0 < \lambda < 1$ and $\delta_0 = \sqrt{2\frac{|\mathbb{S}_\mathbb{B}|}{|B|}}$. Typically, we use $\lambda = 1$ or $\lambda = \frac{1}{2}$ if one can afford a computation time four times longer. The cost function in (9) only depends on three parameters, σ, α, and δ. As discussed, an optimal value can be calculated for them, so actually the cost function can be considered parameter-free.

Recalling that the whole point of our approach is to design a differentiable cost function, the question that naturally arises is the calculation of the gradient of our discrete cost (9) with respect to the positions of the antennas. Even though the expression of the gradient can be computed explicitly, it is much more practical and computationally efficient to use automatic differentiation. This requires encoding C as a composition of differentiable functions. The first step is to encode the operation $A \to B$, which is detailed in Algorithm 1.

Then, for any $u \in G_r$, we have to encode the computation of $\mathbf{d}_\mathbf{B}^{\sigma_1}(u)$, which is done in Algorithm 2.

Using these two functions, one can easily compute the discrete cost (9) as the result of Algorithm 3.

Note that the proposed algorithms are purposely based on basic matrix operations only so they can be implemented with any of the available automatic differentiation libraries.

Finally, one needs to take into account the spatial constraints of the instrument. Indeed, in the final layout, the antennas are expected to lay on the surface $\mathbb{S}_\mathbb{A}$ of the satellite. The shape of the structure depends on what is possible to deploy on space after unfolding the instrument. The square, hexagon, cross, or "Y" (SMOS) shapes have been considered for SMOS-HR and it is indeed a very challenging engineering problem to find the right way to store and unfold the structure.

We express this as the following constrained problem:

$$\min_{A \in \mathbb{S}_\mathbb{A}{}^N} C(A). \tag{11}$$

Thus, we have reduced the original problem to a standard constrained optimization for which a variety of methods can be applied. Comparing the performances of these methods has a potential for future work, and,thus we have only focused on one augmented Lagrangian-like method. This heuristic implies solving a series of nonconstrained problems instead of directly solving (11), an approach that is commonly believed to be a good heuristic for avoiding local minima [22].

The first step in this method is to define a penalty function g such that

$$g(a_i) \begin{cases} = 0 \text{ if } a_i \in \mathbb{S}_\mathbb{A} \\ > 0 \text{ otherwise} \end{cases}. \tag{12}$$

Then, for all $\mu > 0$, we define the unconstrained problem

$$(P(\mu)) : \min C(A) + \mu \sum_{a_i \in A} g(a_i).$$

In this way, a high value of μ induces tight constraints (any antenna outside of S_A produces a strong augmentation of the cost) while a low value of μ would relax to loose constraints. The value of μ is incremented throughout the optimization, so that in the end, $g(A) = 0$ (meaning that the constraints are respected) while keeping the value of $C(A)$ as low as possible. More precisely, we define a finite increasing sequence (μ_n) and we solve $P(\mu_{n+1})$ by gradient descent using as initialization the solution obtained for $P(\mu_n)$, as detailed in Algorithm 4.

The choice of a proper penalty function g is a classic issue in constrained optimization. Here, the squared distance to $\mathbb{S}_\mathbb{A}$ is a natural candidate that checks the required properties, namely

Algorithm 4: Constrained Optimization($\nabla g, \nabla Cost, (\mu_n)_{1:N}, A_0, \eta, n_{\text{sub}}$).

Input: ∇g : the gradient of the penalty function
$\nabla Cost$: the gradient of the Cost function
$(\mu_n)_{1:N}$: the finite increasing sequence $\mathbf{A}_0$: The initialization
η: the learning rate n_{sub}: the number of subiteration n_{sub}
Output: $\mathbf{A}$: optimized position of the antennas
$\mathbf{A} \leftarrow \mathbf{A}_0$
for $n \in 1, .., N$ **do**
  for $k \in 1 \dots n_{\text{sub}}$ **do**
    $\mathbf{A} \leftarrow \mathbf{A} - \eta(\nabla \text{Cost}(\mathbf{A}) + \mu_n \nabla g(\mathbf{A}))$ {GD step}
  end for
end for
return A

being differentiable and easy to compute. Thus, in the following, we simply define

$$g(a_i) = d(a_i, \mathbb{S}_{\mathbb{A}})^2. \tag{13}$$

If we call $P_{\mathbb{S}_{\mathbb{A}}}$ the projection on $\mathbb{S}_{\mathbb{A}}$, we thus have

$$g(a_i) = |a_i - P_{\mathbb{S}_{\mathbb{A}}}(a_i)|^2 \tag{14}$$

and

$$\nabla g(a_i) = 2(a_i - P_{\mathbb{S}_{\mathbb{A}}}(a_i)). \tag{15}$$

The presence of constraints makes the process more complex, as it depends on three additional hyperparameters: the sequence (μ_n), the learning rate η, and the number of subiterations n_{sub}. To make it simpler, we make the classic assumption that $\mu_{n+1} = 2^n \mu_0$. This reduces the definition of the sequence to the parameter μ_0. The visualization of the values taken by $C(A)$ and $g(A)$ through the optimization provides insight on the correct choice of these hyperparameters. Indeed,

- $C(A)$ decays quickly at first because the problem $P(\mu_0)$ has very loose constraints. Then, it increases slowly as the algorithm tries to keep $C(A)$ as low as possible despite the tightening of the constraints. Thus, if $C(A)$ does not decrease quickly at the beginning of the optimization process, it means that μ_0 is too high. If it does not increase afterwards, it means that μ_0 is too low. If μ_0 is set correctly (e.g., $\mu_0 = 0.001$ in our case), the evolution of $C(A)$ is expected to look like as shown in Fig. 7 .
- The choice of the learning rate η is a classic problem in optimization. The goal is to set η at values as high as possible while avoiding oscillations and eventually the divergence of $C(A)$. For the applications considered in this article, our choice is $\eta = 10$.
- Finally, n_{sub} must be as low as possible to control the computational cost, but large enough so that the algorithm converges at each subiteration. This parameter can be easily validated by checking that the evolution of $C(A)$ and $g(A)$ becomes very slow at the end of each subiteration (see Fig. 8).

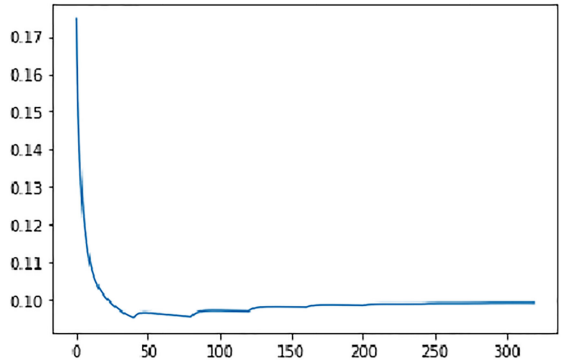

Fig. 7. Evolution of $C(\mathbf{A})$ through the optimization when μ_0 is properly chosen. This plot corresponds to $N = 100$ antennas, $\mu_0 = 0.001$.

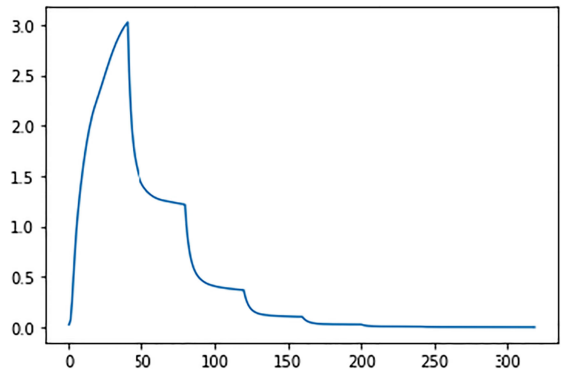

Fig. 8. Evolution of the penalization through the optimization when n_{sub} is properly chosen. The decrease gets really slow at the end of each subiteration.

The typical value for the applications considered in this article is $n_{\text{sub}} = 50$.

IV. Constraints in a Satellite

We now examine the specific problem of optimizing the configuration of an interferometric array supported by a satellite. This situation comes with two major issues: the nonoverlapping spatial constraint for the antennas located on a narrow bar and the calibration of the antennas on an irregular grid.

A. Proximity of the Antennas

In the case of a spaceborne interferometric array, the radii of the antennas are not negligible compared to the size of their supporting frame, and the typical width W of an arm begins typically less than five times the radius R of an antenna. Therefore, avoiding antenna overlaps is both a nontrivial constraint and mandatory to get a feasible configuration. The most direct option would be to turn the gradient descent method into a projected gradient descent on the space of "nonoverlapping antennas." Unfortunately, this projection is both difficult to formalize and computationally expensive. It can be simplified by moving each antenna separately. Instead of computing this projection, we consider the N-nearest neighbors of the single moving antenna and find the largest favorable move such that this antenna does not overlap with its neighbors.

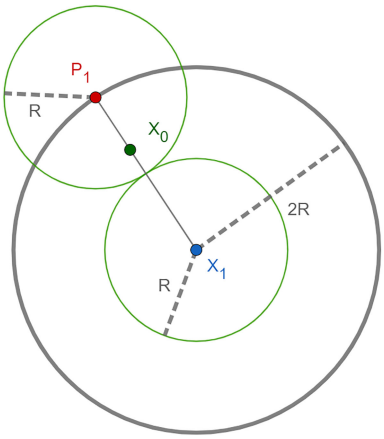

Fig. 9. Computation of 1-NearestNeighborProjector where the antennas X_0 and X_1 are overlapping. P_1 is the projection of X_0.

Algorithm 5: 1-Nearest Neighbor Projector(**A**,R).

Input: $\mathbf{A} \in M_{2,n}(\mathbf{R})$ where n is the number of antennas and $A_{1,i} = a_i^x$, $A_{2,i} = a_i^y$ the coordinates of antenna #i.
R: the radius of each antenna
Output: **A**, resulting configuration of antennas (in-place).
for $i \in 1, .., n$ **do**
  $X_0 = (a_i^x, a_i^y)$
  $X_1 = \arg\min_{j \neq i}(\|X_0 - (a_j^x, a_j^y)\|)$
  if $\|X_0 - X_1\| \leq 2R$ **then**
    $X_0 \leftarrow X_0 + \max\left(\left(\frac{2R}{\|X_0 - X_1\|} - 1\right), 0\right)(X_0 - X_1)$
  {Put away}
    $A_{1,i} = X_{0,1}$
    $A_{2,i} = X_{0,2}$ {Set position of (a_i^x, a_i^y)}
  end if
end for
return A

Fortunately, the layout of antennas produced by our method do not tend to have that many overlapping antennas.[1] Thus, applying the 2-nearest neighbors projection for each antenna at each step of the gradient descent is enough to solve the issue while remaining computationally feasible.

In the following, we expand on the computation of the 1-nearest neighbors and 2-nearest neighbors projectors. We will use the following notations: X_0 is the position of the antenna to move, X_1 and X_2, respectively, are its first and second nearest neighbors, and R is the radius of the antennas. The 1-nearest neighbor correction move is summarized in Fig. 9

or by (16)

$$P_1 = X_0 + \max\left(\left(\frac{2R}{\|X_0 - X_1\|} - 1\right), 0\right)(X_0 - X_1). \tag{16}$$

It can be computed with Algorithm 5.

[1]Because a configuration where the antennas are close is a bad configuration, it tends to be naturally avoided by minimizing the energy in (8).

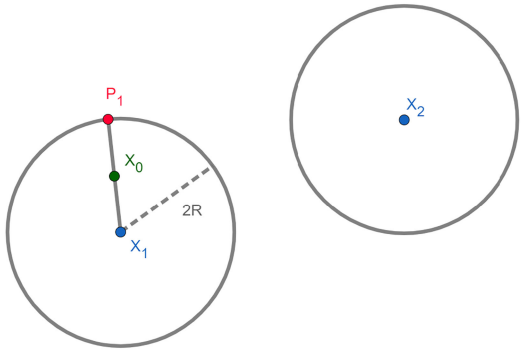

Fig. 10. Case 1 in the computation of the 2-NearestNeighborProjector P_2: $d(P_1, X_2) > 2R$. The solution of the 1-nearest-neighbor-projector is also the solution of the 2-nearest-neighbor-projector.

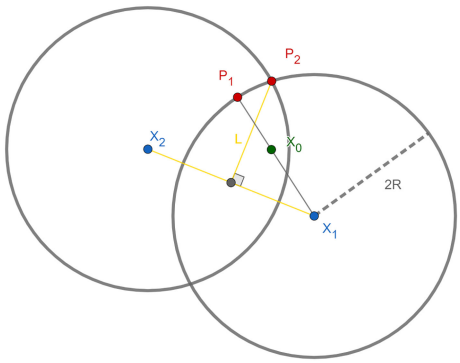

Fig. 11. Case 2 in the computation of the 2-nearest-neighbor-projector P_2: $d(P_1, X_2) < 2R$. The solution of the 1-nearest-neighbor-projector is too close to X_2.

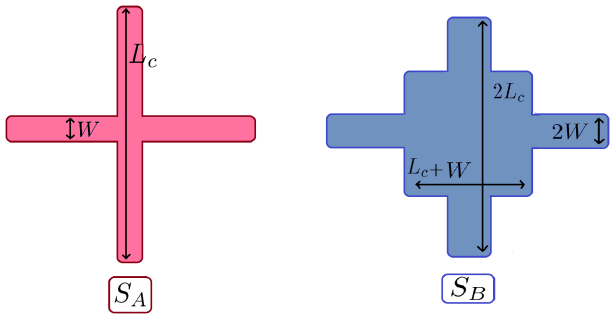

Fig. 12. $\mathbb{S}_{\mathbb{A}}$ and $\mathbb{S}_{\mathbb{B}}$ for a cross-shaped satellite frame.

The 2-nearest neighbor approach is much more efficient and it can be calculated through basic geometric considerations. We summarize it in Figs. 10 and 11.

In the first case, the computation of P_2 is reduced to the computation of P_1, and in the second case, the computation of P_2 involves finding L satisfying

$$(2R)^2 = L^2 + \left\|\frac{X_2 - X_1}{2}\right\|^2$$

so that the updated position of X_0, P_2, will be of distance $2R$ from both neighbors X_2 and X_1.

Thus, it can be performed as described in Algorithm 6.

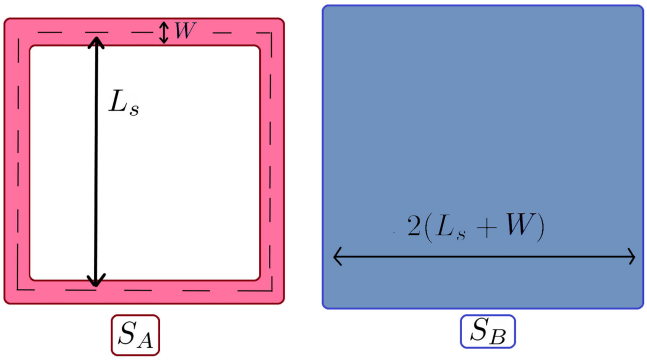

Fig. 13. $\mathbb{S}_{\mathbb{A}}$ and $\mathbb{S}_{\mathbb{B}}$ for a square-shaped satellite frame.

Algorithm 6: 2-Nearest Neighbor Projector(**A**,R).

Input: $\mathbf{A} \in M_{2,n}(\mathbf{R})$ where n is the number of antennas and $A_{1,i} = a_i^x$, $A_{2,i} = a_i^y$ the coordinates of antenna #i. R: the radius of each antenna //

Output: **A**, resulting configuration of antennas (in-place).

for $i \in 1 \dots n$ **do**

$X_0 = (a_i^x, a_i^y)$

$X_1 = \arg\min_{j \neq i}(\|X_0 - (a_j^x, a_j^y)\|)$

if $\|X_0 - X_1\| \leq 2R$ **then**

$X_0 \leftarrow X_0 + \max\left(\left(\frac{2R}{\|X_0 - X_1\|} - 1\right), 0\right)(X_0 - X_1)$

{Put away}

$X_2 = \arg\min_{j \neq i}(\|X_0 - (a_j^x, a_j^y)\|)$ where $X_2 \neq X_1$

$U_1 = \frac{X_2 - X_1}{2} + \sqrt{R^2 - \|\frac{X_1 - X_2}{2}^2\|}\left(\left(\frac{X_2 - X_1}{2}\right)_y, -\left(\frac{X_2 - X_1}{2}\right)_x\right)$

$U_2 = \frac{X_2 - X_1}{2} + \sqrt{R^2 - \|\frac{X_1 - X_2}{2}^2\|}\left(-\left(\frac{X_2 - X_1}{2}\right)_y, \left(\frac{X_2 - X_1}{2}\right)_x\right)$

$X_0 = \arg\min_i \|U_i\|$

$A_{1,i} = X_{0,1}$

$A_{2,i} = X_{0,2}$ { Set position of (a_i^x, a_i^y) }

end if

end for

return A

B. Calibration

Camps *et al.* [23] discussed the problem of the calibration of large antenna arrays in the absence of a beamforming point source, which is a common problem in the beamforming radars and interferometric radiometers. They proposed an iterative method to calibrate the gains in phase and amplitude taking advantage of the fact some baselines are redundant. Their method, called redundant space calibration (RSC), is the base of the SMOS calibration [24]. Taking into account that the baseline redundancy is significantly reduced in the case of irregular array configurations, it is pertinent to ensure that irregular arrays can be calibrated. In the following, it is shown that the RSC can still be applied to irregular arrays if the antennas positions are discretized in a fine grid.

The raw phase of the visibility observation from antennas a_i and a_j is

$$\phi_{i,j}^{\text{raw}} = f_i - f_j + \phi_{i,j} \tag{17}$$

where f_i and f_j give the phase offsets for antennas i and j and $\phi_{i,j}$ gives the phase of the corresponding baseline $(a_i - a_j)$ for the ideal instrument.

The log modulus of the visibility observation can be decomposed in a similar fashion

$$A_{i,j}^{\text{raw}} = G_i + G_j + A_{i,j}. \tag{18}$$

The phase shift of each of the antennas can be determined by solving the system of equations for each pair of antennas with (17) and the gains independently with the system of equations (18). The unknowns are the $f_{(.)}$ (respectively, $G_{(.)}$) and $\phi_{(.,.)}$ (respectively, $A_{(.)}$). The RSC method assumes that $\phi_{i,j} = \phi_{k,l}$ and $A_{i,j} = A_{k,l}$ if $a_i - a_j = a_k - a_l$ (redundant observations of the same baseline should have the same ideal instrument visibility modulus and phase). Therefore, the system of equations can be solved only if each antenna is involved in a visibility that is observed more than once. From now on, we will only refer to equations on the phase shift ϕ, since exactly the same can be applied to the log gains, without loss of generality.

In matrix notation,

$$\phi^{\text{raw}} = (f_1\ f_2\ \dots\ \phi_{1,2}\ \phi_{1,3}\ \dots)\Psi \tag{19}$$

where Ψ is a matrix that contains entries with $+1$ (for f_i and $\phi_{i,j}$) and -1 (for f_j). Each of its columns represents one of the equations of the system.

As Camps *et al.* [23] point out, one can assume that $f_0 = 0$ and refer all the other phase shifts to that reference. Indeed, the system is invariant to adding a global phase-shift constant. Therefore, the system is determined if

$$\text{rank}(\Psi) \geq |f| + |\phi| \tag{20}$$

where $|f| + |\phi|$ is the number of unknowns.

However, in a purely irregular configuration, there is no guarantee that the multiplicity of the visibilities is more than one. Hence, the system of equations is likely to be unsolvable. A simple solution is to introduce increasingly a slight quantization of the position of the antennas, until the system can be calibrated with the condition in (20). To obtain this regularity, we introduce a grid of regular step ϵ on the antennas' plane, thus shifting each antenna to its nearest neighbor on the grid. The optimal ϵ^* is defined by

$$\epsilon^*_{\text{phase}} = \inf_\epsilon \{\epsilon / \text{rank}(\Psi_\epsilon) \geq |f| + |\phi|\} \tag{21}$$

where Ψ_ϵ is the matrix obtained after by fixing a grid of step ϵ. The optimal $\epsilon^*_{\text{phase}}$ is found by a dichotomic search. Moreover, all this approach could also be adapted for the calibration of the gains which will then produce a ϵ^*_{gain}. Then, one should take $\epsilon^* = \max\{\epsilon^*_{\text{phase}}, \epsilon^*_{\text{gain}}\}$ as the global solution.

C. Application to Tentative Successors of SMOS

We optimize the positions of the antennas on several designs envisaged for the higher resolution successors of the SMOS

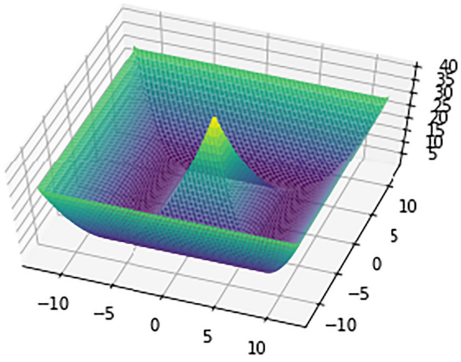

Fig. 14. Penalty function on the domain S_A for a square-shaped frame.

satellite, which we will call *SMOS-HR* [5]–[7], [25], [26]. The optimization problem is fully specified by the shape $\mathbb{S}_{\mathbb{A}}$ of the satellite, the number N of antennas, and their radius R.

In the case of SMOS-HR, we have the following.

- $R = \lambda/2 \approx 0.11$ m (this also includes any minimal barrier distance between antennas).
- $69 \leq N \leq 231$ antennas. The exact number of antennas has not been already set, but certainly SMOS-HR will have more antennas than the current SMOS, and up to 231 antennas.
- Several shapes have been proposed, including the cross with $L_c = 2 \times L_s$ (see Fig. 12) and the square with $L_s = 12m$ (see Fig. 13).[2]
  The width of the frame will be fixed for both $W_s^0 = 5R$ and $W_c^0 = W_s^0$. This implies that the centers of the antennas are constrained to a width $W = W_s^0 - 2R$ (respectively, W_c^0).

From these quantities, one can easily deduce the other characteristics of the problem, such as $\mathbb{S}_{\mathbb{B}}$, δ_0, and σ_0.

In both cases, it is also easy to explicitly compute the penalty function and its gradient [see (14) and (15)]. Indeed, in both cases, one can easily compute the projection $P_{\mathbb{S}_{\mathbb{A}}}$ on $\mathbb{S}_{\mathbb{A}}$. If we write $a = (a_x, a_y)$ the position of the antenna and we assume that $a_x > a_y \geq 0$ without loss of generality, in the case of the square, we have

$$P_{\mathbb{S}_{\mathbb{A}}}(a_x, a_y) = \left(\min\left(\frac{L_s}{2} + \frac{W_s}{2}, a_x\right) \max\left(\frac{L_s}{2} - \frac{W_s}{2}, a_y\right)\right).$$

In the case of the cross, we have

$$P_{\mathbb{S}_{\mathbb{A}}}(a_x, a_y) = \left(\min\left(\frac{L_s}{2}, a_x\right), \min\left(\frac{W_s}{2}, a_y\right)\right).$$

The associated penalty function is represented in Fig. 14 for the square frame.

[2]These two quantities have in common the associated satellite can carry the same number of antennas in the case of a regular layout.

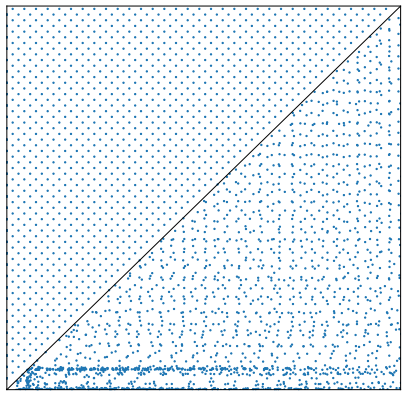

Fig. 15. Comparison of the $u - v$ plane sampling of the quincunx configuration and the optimized irregular configuration on the square frame. The baselines of the quincunx configuration are displayed on the upper left corner, while the baselines of our optimized configuration on the irregular square frame are displayed on the bottom right for comparison. We can observe that we have almost twice as many distinct sampling points within the same area with the irregular configuration as we do with the quincunx (see Table I).

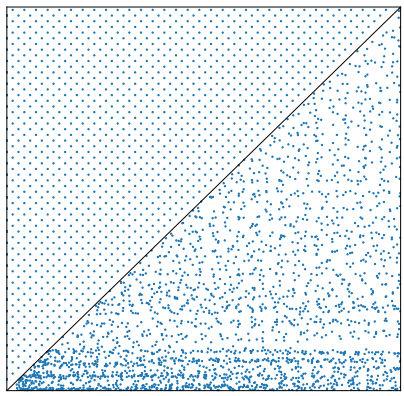

Fig. 16. The same as Fig. 15, except that the irregular configuration is our optimized cross. We can then observe that we have almost twice as many sampling points within the same area (see Table I).

V. Results and Analysis

A. Results: Layouts

We have applied our method to the two candidates for the shape of the SMOS-HR: the square and the cross. The number of antennas in SMOS-HR has not been yet decided, but certainly it will be more than the 69 antennas in the current SMOS instrument, and up to 231 antennas. The method we present in this article is general and can be adapted to different frame shapes and number of antennas. In our simulations, we have used 180 antennas.

Appendix A shows the layouts we have obtained for the two regular configurations which are currently being considered for SMOS-HR (irregular cross in Fig. 23, and irregular square in Fig. 24), along with the quincunx cross (Fig. 22). The quincunxes consist of satellites with regularly placed antennas and half an arm shifted by (R, R), where R is the radius of the antennas.[3]

[3]Note that the square and cross quincunxes as presented here are really effective configurations in terms of coverage of the $u - v$ plane, but are not

In Appendix B, we show the baselines in detail (quincux in Fig. 25, our solution on the cross in Fig. 26, and our solution on the square in Fig. 27).

B. The Kernel of Each Configuration

Here we develop a visual representation of the quality of a layout.

Recall that, according to (2), an ideal observation would be $\mathbf{V} = \mathbf{F}(\widetilde{T})$. Yet the observed visibilities are restricted to the sparse set

$$V_{\mathbf{B}} = \{\mathbf{V}(\nu_b) \text{ for } b \in \mathbf{B}\} \tag{22}$$

where $\mathbf{B}$ is the set of baselines and $\mathbf{V}(\nu_b)$ the Fourier transform evaluated at $\nu_b = \frac{b}{\lambda}$, associated with the baseline b. Thus, we have only access to the pseudo-Dirac comb

$$\mathbf{V}_{\mathbf{B}}^{\alpha} = \mathbf{V}.\sum_{b\in\mathbf{B}} \alpha_b \delta_{v_b} \tag{23}$$

where α_b is a weight associated with the visibility observed in b, which we add to compensate for local visibility redundancy. Hence, the reconstruction of the signal can be described as the operation

$$\widetilde{T}_r = \boldsymbol{\mathcal{F}}^{-1}\{\mathbf{V}_{\mathbf{B}}^{\alpha}\}. \tag{24}$$

Thus, in order to get a good approximation $\widetilde{T}_r \approx \widetilde{T}$, we need to have that $\mathbf{V}_B^{\alpha} \approx \mathbf{V}$ at least on $\frac{1}{\lambda}\mathbb{S}_{\mathbb{B}}$. Therefore, the quality of the reconstruction depends on the quality of the approximation

$$\sum_{b\in\mathbf{B}} \alpha_b \delta_{u_b} \approx \mathbb{1}_{\frac{1}{\lambda}\mathbb{S}_{\mathbf{B}}}.$$

This approach confirms the intuition that a uniform distribution of the baselines provides to the best reconstruction. Indeed, in that case, a constant weight $\alpha_b = \frac{|\frac{1}{\lambda}\mathbb{S}_{\mathbb{B}}|}{|B|}$ provides an efficient approximation. In the general case, one must compensate the fact that some areas might be oversampled and other subsampled by modifying the weight accordingly. Fortunately, we have access to a metric to estimate this notion of density that makes sense within the framework of this article, namely $\mathbf{d_B}$. Thus, in the following, we simply use

$$\alpha_b = \frac{\mathbf{d_B}(b,\sigma)}{\sum \mathbf{d_B}(b,\sigma)} \left|\frac{1}{\lambda}\mathbb{S}_{\mathbb{B}}\right|. \tag{25}$$

By classic properties of the Fourier transform, we have

$$\widetilde{T}_r = \boldsymbol{\mathcal{F}}^{-1}\{\mathbf{V}_B^{\alpha}\} = \boldsymbol{\mathcal{F}}^{-1}\{\mathbf{V}\} * \boldsymbol{\mathcal{F}}^{-1}\left\{\sum_{b\in B} \alpha_b \delta_{u_b}\right\}$$

$$\widetilde{T}_r = \widetilde{T} * \mathbf{K} \tag{26}$$

where $\mathbf{K} = \boldsymbol{\mathcal{F}}^{-1}\{\sum_{b\in B} \alpha_b \delta_{\nu_b}\} = \sum_{b\in B} \alpha_b e^{-2i\pi\nu_b}$ is the kernel, which quantifies the quality of the reconstruction. The ideal kernel would of course be the Dirac mass $\delta_{0,0}$.

Since $\widetilde{T}$ has a compact support that is the disc $D_1 = \{(\xi,\eta) \in \boldsymbol{\mathcal{R}}^2$, such as $||(\xi,\eta)||_2 < 1\}$, it only matters to plot $\mathbf{K}$ in $D_2 = \{(\xi,\eta) \in \boldsymbol{\mathcal{R}}^2$, such as $||(\xi,\eta)||_2 < 2\}$, to give the local weights with which $\widetilde{T}$ is averaged in the convolution operation.

feasible because two antennas overlap. Still, we consider these since they provide the ideal achievable frequential coverage with regular configurations.

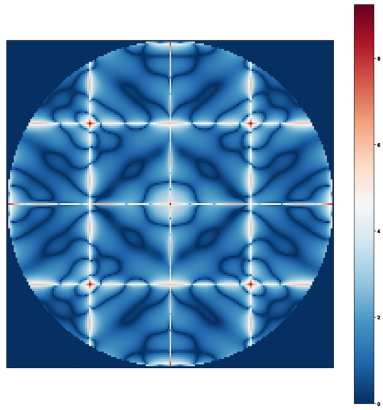

Fig. 17. $\log(1+|K|)$, where K is the kernel of the regular configuration (on the square). The kernel exhibits four parasite Dirac in $(\pm1,\pm1)$ induced by coherent aliasing; these Dirac have the same mass as the central Dirac which imply a strong image folding.

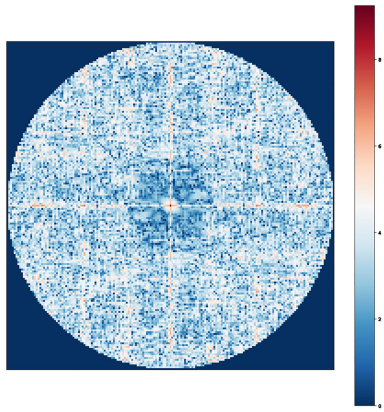

Fig. 18. $\log(1+|K|)$, where K is the kernel of the irregular configuration (on the square). The kernel exhibits unstructured noise which adds a reconstruction error, but not spatial folding.

Plotting the kernels yields an understanding of the efficiency of the different configurations. As shown in Fig. 17, the kernel associated with the quincunx configuration exhibits four parasite Dirac in $(\pm1,\pm1)$ and thus reduces to

$$K_{qcx} = \delta_0 + \sum_{(i,j)\in(\pm1,\pm1))} \delta_{(i,j)}. \tag{27}$$

The reconstruction associated with such kernel exhibits a nonfolded area $\{x \ / \ \widetilde{T} * K(x) = \widetilde{T}(x)\}$ with low error and a folded area where the information is lost. As illustrated in Fig. 19, the folding causes a loss of 73% of the information. Conversely, Fig. 18 shows the kernel of an irregular layout, where there is no folding structure but a "dirty image" instead (replicas of the images centered at each of the sampling points). This confirms that the intrinsic flaw of the regular configurations, namely its image folding, can be amended by using an irregular array. The fraction of the information irrevocably lost in the case of the quincunx (see Fig. 19) is available with the irregular array, at the cost of more noise in the reconstruction.

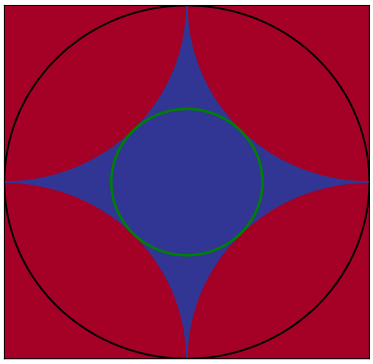

Fig. 19. Folding with the quincunx array. The black circle represents the D_1 disc in which the information is located, i.e., in which $\widetilde{T}$ is not null. The nonfolded area Π is in blue, while the folded area due to the parasite dirac is in red. A fraction $1 - \frac{|\Pi|}{|D_1|} = \frac{2\pi-4}{\pi} = 0.73$ of the information is irrevocably lost because of the folding. The green circle represents the largest discussed $D_{\rho_{\max}}$ in the nonfolded area, $\rho_{\max} = \sqrt{2} - 1 \approx 0.41$.

C. Inversion

To compare the efficiency of the different layouts, we shall compare the results of the image reconstruction from visibilities in the presence of noise. In order to obtain the reconstructed image via our antennas's layout, one needs to define the number of pixels that should be used for the reconstruction. We have $\nu_{i,j} = \frac{a_i - a_j}{\lambda}$, where $\lambda = 2R \approx 0.21$ cm is within the L-band. $\nu^u_{i,j}$ and $\nu^v_{i,j}$ are the two components of the baseline vector in the $u - v$ frequency plane. The size of the reconstruction size is given by the maximum sampling frequency

$$f_{\max_u} = \max_{i,j} \nu^u_{i,j} - \min_{i,j} \nu^u_{i,j}$$

and

$$f_{\max_v} = \max_{i,j} \nu^v_{i,j} - \min_{i,j} \nu^v_{i,j}.$$

We obtain

$$N_{\text{pixel}} = f_{\max_u} \times f_{\max_v}.$$

In the following, we will write N_x and N_y for the number of pixels, respectively, along the X- and Y-axes of the reconstructed image. Thus, according to the previous reasoning, the right choice is $N_x = f_{\max_u}$ and $N_y = f_{\max_v}$. The first step of the reconstruction is then to discretize (1) as

$$V_{\nu_{i,j}}(u,v) = \frac{4}{N_x N_y} \sum_{x=0}^{N_x-1} \sum_{y=0}^{N_y-1} T[\xi,\eta] F_{i,j}[\xi,\eta] \times \exp\left(-2i\pi\nu^u_{i,j}\xi - 2i\pi\nu^v_{i,j}\eta\right) \quad (28)$$

where $\xi = 2(x - \frac{N_x}{2})/N_x$ and $\eta = 2(y - \frac{N_y}{2})/N_y$. Viewing $V_{i,j}[u,v]$ as a vector of dimensions $|\mathbf{B}|$ (the number of baselines) and $\widetilde{T}$ as a vector of dimensions $N_x \times N_y$, we can write this system of equations as

$$V = GT. \quad (29)$$

In the ideal noiseless case, when in addition the ARPs of the antennas are equal and perfectly known and all baselines are regularly placed, (28) reduces to a simple discrete Fourier transform. G is then a Fourier matrix and the reconstruction of $\widetilde{T}$ is the result of an inverse discrete Fourier transform. To obtain the brightness temperatures from the visibilities, one needs to solve the minimization problem in (30). It can be solved directly by a least squares method. Although if the brightness temperature needs to be obtained directly on board (like in the case of SMOS), a Moore–Penrose pseudo-inverse is preferred because of computation timing constraints.

$$T_r = \arg\min_T ||V - GT||_2^2. \quad (30)$$

TABLE I
CALIBRATION STEP GRID AND THE NUMBER OF VISIBILITIES FOR THE DIFFERENT CONFIGURATIONS

	Calibration step grid ϵ (m)	Number of visibilities
Irregular square	0.031	31577
Irregular cross	0.020	31915
Quincunx square	0	18549
Quincunx cross	0	17777

We evaluated the reconstructions obtained with the quincunx and the irregular configurations (with the square and cross shapes in both cases). The level of noise added is governed by (3), and the parameters are $B = 20$ MHz bandwidth and $\tau = 2$ s integration time.

1) Simple and Complex Scene: We used two different ground-truth scenes: a disk representing a body of constant 300 K temperature and 0 K outside the disc, and a map of brightness temperatures of the Earth, containing the oceans at 90 K (not constant, but with SD=1) and the continents.

We call these scenes, respectively, the *simple* and the *complex* scenes. They are not meant to be realistic scenes of the brightness temperature of the Earth in the L-band, but retain similar variations and contrast. The simple scene has an abrupt change when it goes from 300 K to 0 K, which is useful to evaluate the behavior of the instrument in the presence of extreme signal changes. The complex scene allows for testing with a scene with values of brightness temperatures close to the expected ones in both the oceans and continents, with smooth and fast variations. Using this setting, we evaluated the performance of our layouts in terms of root mean squared error (RMSE) and show the reconstructed brightness temperature maps, as well as the difference with the ground-truth.

Since the reconstruction provided by the quincunx configuration (as well as any regular one, due to the minimal distance between antennas and the nonoverlapping constraint) are necessarily folded, we limit the RMSE evaluation to the unfolded zone. Thus, we compared the two different RMSEs in the inner disc $D_{\rho_{\max}}$, where $\rho_{\max} = \sqrt{2} - 1$ is the maximal radius possible for the disc in which no folding occurs, as illustrated in Fig 19. Thus, we define our RMSE in the nonfolded area as

$$\text{RMSE}(T_r, T) = \sqrt{\text{mean}_{i,j}([T_r[i,j] - T[i,j]^2)}, (i,j) \in D_{\rho_{\max}}. \quad (31)$$

Table II gives the RMSEs for the reconstruction of the simple and complex scenes, the size of the reconstruction in pixels, and the angular resolution in radians, for all the tested configurations.

TABLE II
RMSEs FOR THE RECONSTRUCTION OF THE SIMPLE AND COMPLEX SCENES, THE SIZE OF THE RECONSTRUCTION IN PIXELS, AND THE ANGULAR RESOLUTION IN RADIANS, FOR ALL THE TESTED CONFIGURATIONS

	Simple	Complex	Rec. size	Angular res.
Irregular square	8.66 K	3.65 K	191×191	0.016 rads
Irregular cross	13.17 K	5.83 K	191×191	0.011 rads
Quincunx square	2.18 K	1.19 K	182×184	0.016 rads
Quincunx cross	2.52 K	2.47 K	188×190	0.011 rads

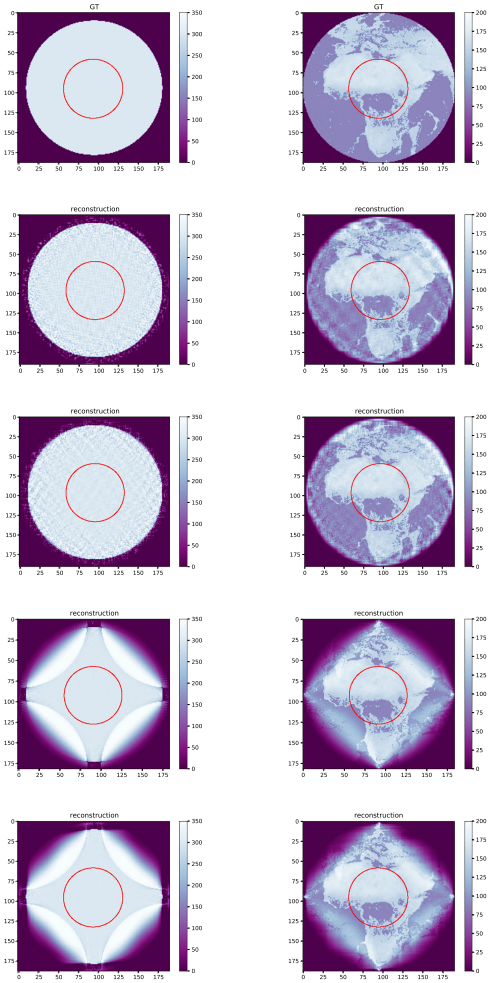

Fig. 20. First column: Results on the simple scene (body at constant 300 K temperature). Second column: Results on the complex scene. First row: Original scene (ground truth). Second row: Irregular cross. Third row: Irregular square. Fourth row: Quincunx square. Fifth row: Quincunx cross. The red circle represents the edge of the unfolded $D_{\rho_{\max}}$ disc.

The angular resolution is calculated as λ/D, where D is the diameter of the instrument (the largest distance between two antennas). Fig. 20 shows the obtained reconstruction with each of the layouts.

2) Simulation of Failures in the Antennas: Each of the antennas comes along with the electronic circuitry (amplifiers, accurate filters, etc.), which is prone to failures. Failures could happen, given that SMOS is now beyond twice its expected 5-years planned lifetime.

We simulated a failure of 7% of the antennas in the instrument. If such an event should happen, the G matrix and its pseudo-inverse would be recomputed to take into account the new layout

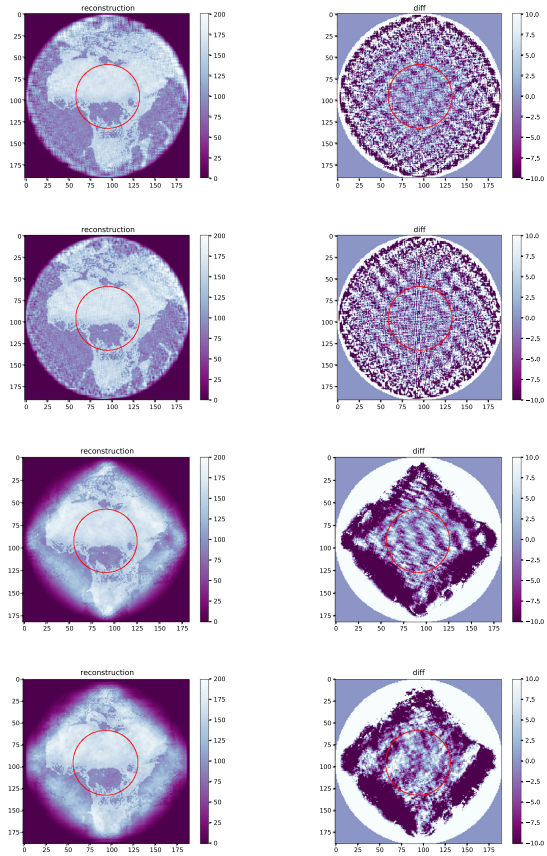

Fig. 21. Left column: Reconstruction with the irregular square, irregular cross, quincunx square, and quincunx cross with 7% antenna failure. Right column: Reconstruction error (difference between ground-truth and reconstruction). The perfect regularity of the quincunx is lost when some antennas fail, thus the reconstruction artifacts approaching to those of the irregular configurations.

TABLE III
RMSE OBTAINED WITH EACH OF THE CONFIGURATIONS, WITHOUT ANY FAILURES (LEFT) AND WITH 7% OF THE ANTENNAS FAILING, FOR THE "COMPLEX" SCENE

	RMSE normal	RMSE failures
Irregular square	3.66 K	5.36 K
Irregular cross	5.82 K	7.20 K
Regular square	1.22 K	5.00 K
Regular cross	2.47 K	5.93 K

The error approaches that of the irregular configurations in the event of failures

of antennas. In the case of regular configurations, the perfect regularity of the instrument is lost, therefore approaching an irregular sampling. Fig. 21 shows the reconstructions and the error images.

Table III gives the RMSEs of the configurations. Our evaluation confirms that the RMSE of the reconstruction after simulating the failure of some antennas in the quincunx configuration is close to the RMSE of the irregular configuration. However, there is a fundamental difference in these two cases: in the quincunx and any other regular configuration, the antennas were located on a regular grid and the axes of the DFT are orthogonal. This means that there is no way to recover the missing information from other visibilities. This limitation is not present in the irregular configuration, where interpolation is possible. This

is a significant advantage of the irregular layouts in terms of robustness with respect to the regular configurations, such as the quincunx or the current SMOS.

VI. Conclusion

Missions such as SMOS, SMAP, and Aquarius are useful for a wide range of applications, well beyond the nominal product (SMOS).

The SMOS was launched in 2009. While SMOS is still fully operational, it has gone beyond its planned life time. Its next-generation higher resolution version (SMOS-HR) is under study.

In this article, we have addressed the problem of optimizing the positions of antennas for a spaceborne interferometric array. The methods presented here are general and have been applied here to a tentative design of the future SMOS-HR. We have proposed a new method to optimize the array of antennas on an irregular grid, yet calibrable with a simple procedure.

The most obvious advantage of the irregular layout is that it is not classically folded, as happens with regular configurations. In the case of a regular configuration, the information in the folded area is completely lost, whereas in the case of the irregular layout, one gets a complete reconstruction in the $\xi - \eta$ plane, with a thin noninvertible ring close to the border due to the amplification of the noise by the antennas' ARP. Besides, irregular layouts can achieve a more dense coverage of the $u - v$ plane with the same number of antennas. On the other hand, the irregular layout has a higher reconstruction error (however unstructured) with respect to the regular configurations.

Moreover, we showed that such an irregular array can be calibrated using the same methods as for regular arrays.

We also simulated the effect of failures in the antennas in both types of configurations. Any component in the instrument has a certain probability of permanent failure after its expected useful lifetime. When a failure in one or more antennas happens, the perfect regularity of the instrument is lost and its sampling becomes irregular. Our evaluation confirms this. We proved that the RMSE of the reconstruction after simulating the failure of some antennas in the quincunx configuration is close to the RMSE of the irregular configuration. However, there is a fundamental difference between both sorts of configurations: in the quincunx or in any other similar regular configuration, the antennas are located on a regular grid and the axes of the discrete DFT are orthogonal. This means that there is no way to recover the missing information from other visibilities. This limitation is not present in the irregular configuration, where interpolation remains feasible. This is a significant advantage of the irregular layouts in terms of robustness with respect to the regular configurations, such as the quincunx or the current SMOS.

As future work, we aim to find regularization methods for the inversions that are better than a simple cutoff of the singular values of the G matrix or a mere Tikhonov regularization. Indeed, the larger the G matrix, the more numerically unstable and sensitive to noise the reconstruction. There is room for mathematical research on this problem. Another research direction is the denoising of the snapshots acquired by the instrument. A potential approach would take advantage of the knowledge of the kernel of the impulse of the instrument (in our irregular solution, it mainly appears in the form of unstructured noise) to deconvolve it. A second approach would be to exploit the fact that the satellite takes overlapping snapshots of the Earth as it orbits around, making it possible to fuse them to reduce the noise. Moreover, given that the alias-free FOV is larger with the irregular layout, the multisnapshot approach seems to be well adapted.

Appendix A Antennas Layouts

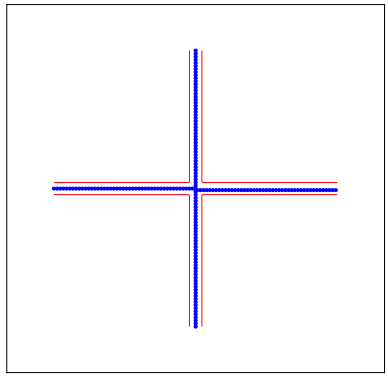

Fig. 22. Quincunx configuration, which has been considered in several projects for successors of SMOS.

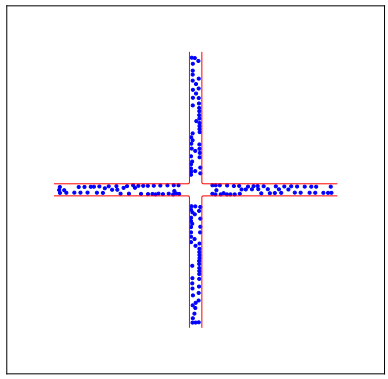

Fig. 23. Optimized irregular configuration of antennas for the cross.

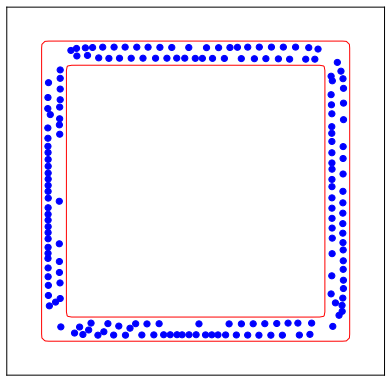

Fig. 24. Optimized irregular configuration of antennas for the square.

APPENDIX B FULL BASELINES LAYOUTS

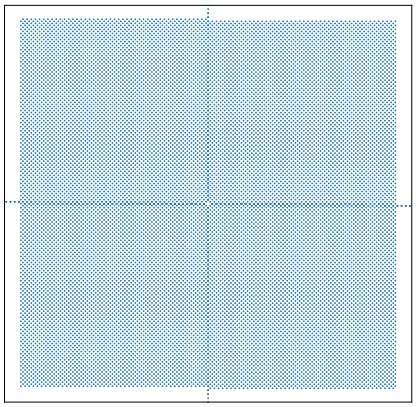

Fig. 25. Baselines associated with the quincunx configuration.

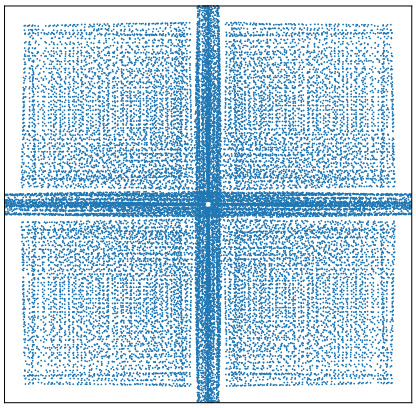

Fig. 26. Baselines associated with our optimized cross configuration.

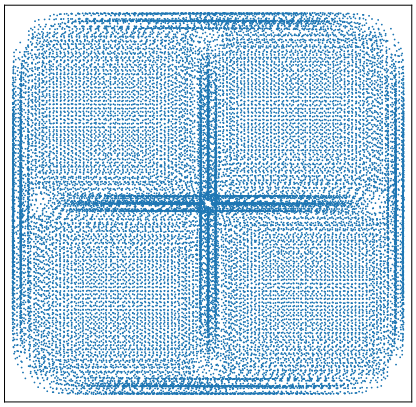

Fig. 27. Baselines associated with our optimized square configuration.

ACKNOWLEDGMENT

The authors would like to thank CESBIO and CNES (R&T CNES 170659/00), as well as École Normale Supérieure Paris-Saclay for their support. The authors acknowledge helpful advice from Alain Trouvé.

REFERENCES

[1] R. Hollmann *et al.*, "The ESA climate change initiative: Satellite data records for essential climate variables," *Bull. Amer. Meteorological Soc.*, vol. 94, no. 10, pp. 1541–1552, 2013.
[2] Y. H. Kerr *et al.*, "The SMOS mission: New tool for monitoring key elements of the global water cycle," *Proc. IEEE*, vol. 98, no. 5, pp. 666–687, May 2010.
[3] Y. H. Kerr, P. Waldteufel, J.-P. Wigneron, J. Martinuzzi, J. Font, and M. Berger, "Soil moisture retrieval from space: The soil moisture and ocean salinity (SMOS) mission," *IEEE Trans. Geosci. Remote Sens.*, vol. 39, no. 8, pp. 1729–1735, Aug. 2001.
[4] Y. H. Kerr *et al.*, "The SMOS soil moisture retrieval algorithm," *IEEE Trans. Geosci. Remote Sens.*, vol. 50, no. 5, pp. 1384–1403, May 2012.
[5] N. J. Rodríguez-Fernández *et al.*, "SMOS-HR: A high resolution L-band passive radiometer for earth science and applications," in *Proc. IEEE Int. Geosci. Remote Sens. Symp.*, 2019, pp. 8392–8395.
[6] Y. H. Kerr *et al.*, "The next generation of L band radiometry: User's requirements and technical solutions," in *Proc. IEEE Int. Geosci. Remote Sens. Symp.*, 2020, pp. 5974–5977.
[7] N. J. Rodriguez-Fernandez *et al.*, "A new L-band passive radiometer for earth observation: SMOS-high resolution (SMOS-HR)," in *Proc. IEEE Int. Geosci. Remote Sens. Symp.*, 2020, pp. 5978–5981.
[8] A. R. Thompson, J. M. Moran, and G. W. Swenson, "Van Cittert-Zernike theorem, spatial coherence, and scattering," in *Interferometry and Synthesis in Radio Astronomy*. Cham, Switzerland: Springer, 2017, pp. 767–786.
[9] C. S. Ruf, C. T. Swift, A. B. Tanner, and D. M. Le Vine, "Interferometric synthetic aperture microwave radiometry for the remote sensing of the earth," *IEEE Trans. Geosci. Remote Sens.*, vol. 26, no. 5, pp. 597–611, Sep. 1988.
[10] A. Moffet, "Minimum-redundancy linear arrays," *IEEE Trans. Antennas Propag.*, vol. 16, no. 2, pp. 172–175, Mar. 1968.
[11] E. Keto, "The shapes of cross-correlation interferometers," *Astrophysical J.*, vol. 475, no. 2, pp. 843–852, 1997.
[12] T. J. Cornwell, "A novel principle for optimization of the instantaneous fourier plane coverage of correction arrays," *IEEE Trans. Antennas Propag.*, vol. 36, no. 8, pp. 1165–1167, Aug. 1988.
[13] H. M. J. P. Barré, B. Duesmann, and Y. H. Kerr, "SMOS: The mission and the system," *IEEE Trans. Geosci. Remote Sens.*, vol. 46, no. 3, pp. 587–593, Mar. 2008.
[14] N. Jin and Y. Rahmat-Samii, "Analysis and particle swarm optimization of correlator antenna arrays for radio astronomy applications," *IEEE Trans. Antennas Propag.*, vol. 56, no. 5, pp. 1269–1279, May 2008.
[15] P. J. Hall, R. T. Schillizzi, P. E. F. Dewdney, and T. J. W. Lazio, "The square kilometer array (SKA) radio telescope: Progress and technical directions," *Int. Union Radio Sci.*, vol. 236, pp. 4–19, 2008.
[16] F. Boone, "Interferometric array design: Optimizing the locations of the antenna pads," *Astron. Astrophys.*, vol. 377, no. 1, pp. 368–376, 2001.
[17] B. Mills and A. Little, "A high-resolution aerial system of a new type," *Australian J. Phys.*, vol. 6, no. 3, pp. 272–278, 1953.
[18] G. Oliveri, F. Caramanica, and A. Massa, "Hybrid ADS-based techniques for radio astronomy array design," *IEEE Trans. Antennas Propag.*, vol. 59, no. 6, pp. 1817–1827, Jun. 2011.
[19] Y. Su, R. D. Nan, B. Peng, N. Roddis, and J. Zhou, "Optimization of interferometric array configurations by 'sieving' U-V points," *Astron. Astrophys.*, vol. 414, no. 1, pp. 389–397, 2004.
[20] M.de Villiers, "Interferometric array layout design by tomographic projection," *Astron. Astrophys.*, vol. 469, no. 2, pp. 793–797, 2007.
[21] F. Boone, "Interferometric array design: Distributions of Fourier samples for imaging," *Astron. Astrophys.*, vol. 386, no. 3, pp. 1160–1171, 2002.
[22] A. Blake and A. Zisserman, *Visual Reconstruction*. Cambridge, MA, USA: MIT Press, 1987.
[23] A. Camps, F. Torres, P. Lopez-Dekker, and S. Frasier, "Redundant space calibration of hexagonal and Y-shaped beamforming radars and interferometric radiometers," *Int. J. Remote Sens.*, vol. 24, no. 24, pp. 5183–5196, 2003.
[24] M. A. Brown, F. Torres, I. Corbella, and A. Colliander, "SMOS calibration," *IEEE Trans. Geosci. Remote Sens.*, vol. 46, no. 3, pp. 646–658, Mar. 2008.
[25] N. Rodriguez-Fernandez *et al.*, "A follow-up for the soil moisture and ocean salinity mission," in *Proc. Copernicus Meetings*, 2021. [Online]. Available: https://ui.adsabs.harvard.edu/abs/2021EGUGA..23.4796R/exportcitation

[26] É. Anterrieu *et al.*, "Preliminary system studies on a high-resolution SMOS follow-on: SMOS-HR," in *Proc. IEEE Int. Geosci. Remote Sens. Symp.*, 2019, pp. 8451–8454.

Paul Krzakala received the B.Sc. degree in mathematics in 2020, from École Normale Supérieure Paris-Saclay, Cachan, France, where he is currently working toward the M.Sc. degree in mathematics.

Amine Assouel received the B.Sc. degree in mathematics in 2020, from École Normale Supérieure Paris-Saclay, Cachan, France, where he is currently working toward the M.Sc. degree in mathematics.

Max Dunitz received the B.S. degree in mathematics and in electrical engineering and computer science and the M.Eng. degree in electrical engineering and computer science from the Massachusetts Institute of Technology, Cambridge, MA, USA, in 2014 and 2016, respectively, and the master's degree in applied mathematics, computer vision, and machine learning in 2019 from the École Normale Supérieure Paris-Saclay in Gif-sur-Yvette, Cachan, France, where he is currently working toward the Ph.D. degree in mathematical design of a new interferometric satellite observing soil moisture.

Eric Anterrieu (Member, IEEE) was born in Brive, France, in 1965. He received the engineering and M.S. degrees in solid-state physics from the Institut National des Sciences Appliquées de Toulouse, Toulouse, France, in 1988 and the M.S. and Ph.D. degrees in image reconstruction in astronomy from University Paul Sabatier, Toulouse, France, in 1989 and 1992, respectively.

Since 1993, he has been an Engineer of Research in Computer Science with the Centre National de la Recherche Scientifique, Paris, France. From 1993 to 2000, he was with the Radio and Optical Aperture Synthesis Group, LATT (UMR 5572), from 2000 to 2004, he was with the Signal and Image Processing Team, Centre Europeen de Recherche et de Formation Avancee en Calcul Scientifique (URA 1875), Toulouse, France, and from 2005 to 2016, he was with the Signal, Image and Instrumentation Group, Institut de Recherches en Astrophysique et Planetologie (UMR 5277), Toulouse, France. Since 2017, he has been with the Observing Systems Team, Centre d'Etudes Spatiales de la Biosphere (UMR 5126), Toulouse, France. His research interests include numerical analysis and image and signal processing, with a focus on the SMOS mission and the future microwave missions using aperture synthesis and interferometry.

François Cabot received the Ph.D. degree in optical sciences from the University of Paris-Sud, Orsay, France, in 1995.

Between 1995 and 2004, he was with the Wide Field of View Instruments Quality Assessment Department, CNES, working on absolute and relative calibration of CNES-operated optical sensors over natural terrestrial targets. In 2004, he joined the Center for the Study of the BIOsphere, Toulouse, France, as an SMOS System Performance Engineer. He has been a Principal Investigator or Coinvestigator for various calibration studies for MSG, Terra, ENVISAT, and ADEOS-II. His research interests include radiative transfer both optical and microwave and remote sensing of terrestrial surfaces.

Ali Khazaal was born in Lebanon, in 1981. He received the engineering degree in telecommunication and computer science from the Faculty of Engineering, Lebanese University, Beirut, Lebanon, in 2003, the M.S. degree in signal, image, acoustic, and optimization from the Institut National Polytechnique, Toulouse, France, in 2006, and the Ph.D. degree in signal/image processing and optimization from University Paul Sabatier, Toulouse, France, in 2009, where he worked with the Signal, Image and Instrumentation Group, Laboratoire d'Astrophysique de Toulouse-Tarbes, Observatoire Midi-Pyrénées.

From 2009 to 2018, he was a Research Scientist with the Centre d'Etudes Spatiales de la BIOsphére, Toulouse, France. In 2019, he started his own company "RDIS Conseils" and specialized in the research and development in spatial imaging. His research interests include numerical analysis and signal and image processing with direct application on ESA's SMOS mission.

Dr. Khazaal is currently a member of the ESA's SMOS Payload Calibration Committee. He is also working on the future microwave missions using aperture synthesis and in particulary CNES's SMOS-HR Project.

Nemesio Rodriguez-Fernandez received the Licentiate degree in fundamental physics and the Ph.D. degree in astrophysics from Universidad Complutense de Madrid, Madrid, Spain, 1996 and 2002, respectively. From 2002 to 2004, he was a Marie Curie Fellow with Observatoire de Paris, Paris, France. From 2004 to 2006, he was a Teaching Assistant with Paris Diderot University, Paris, France, and University of Bordeaux I, Bordeaux, France. From 2006 to 2011, he was an Astronomer with the Institut de Radio Astronomie Milimetrique, Grenoble, France. He is currently a Scientist with Centre d.Etudes Spatiales de la BIOsphre, Toulouse, France. His research interests include microwave remote sensing in astronomy and Earth observation (aperture synthesis algorithms, galaxy dynamics, interstellar chemistry, and soil moisture).

Bernard Rougé received the Ph.D. degree in probabilities from Institut Henry Poincare, Paris, France, in 1975, and the Habilitation a diriger des Recherches degree from Universite de Paris-Dauphine, Paris, France, in 1997. After a long career as an Engineer with the French Space Agency (CNES), he became Emeritus Researcher with CESBIO (Toulouse) and CMLA (Cachan), France. His main research interest is a global approach to the quality of space imagery (sampling, restoration, and compression).

Jean-Michel Morel is currently working toward the Ph.D. degree with Université Paris IV, Paris, France.

He is/was a Postdoc with Scuola Internazionale Superiore di Studi Avanzati, Trieste, Italy, a Teaching Assistant with Université de Marseille Luminy, Marseille, France, an Assistant Professor with Université Paris Dauphine, Paris, France. He is currently a Professor with Ecole Normale Supérieure Paris-Saclay, Cachan, France. For 20 years, he was a permanent Visiting Professor with Universitat de les Illes Balears, Palma, Spain, and a Recurrent Invited Professor with the University of California, Los Angeles, Los Angeles, CA, USA, and Duke University, Durham, NC, USA. His research interests include mathematical theory, and the algorithms of image analysis and image processing.

Dr. Morel was the recipient of the Grand Prix INRIA – French Academy of Science 2013, the CNRS Médaille de l'Innovation 2015, and the Doctor Honoris Causa of U. de la República Montevideo 2018.

Yann H. Kerr (Member, IEEE) received the engineering degree from Ecole Nationale Supérieure de l'Aéronautique et de l'Espace, Toulouse, France, the M.Sc. degree in electronics and electrical engineering from Glasgow University, Glasgow, U.K., in 1977, 1981, and the Ph.D. degree in astrophysique géophysique et techniques spatiales from Université Paul Sabatier, Toulouse, France, in 1992.

From 1980 to 1985, he was with Centre National d'études Spatiales, Paris, France. In 1985, he joined LERTS, where he was the Director from 1993 to 1994. From 1987 to 1988, he was with Jet Propulsion Laboratory, Pasadena, CA, USA, for 19 months. Since 1995, he has been with Centre d'Etudes Spatiales de la Biosphere, Toulouse, France, where he was the Deputy Director from 1995 to 1999 and the Director from 2007 to 2016. His research interests include the theory and techniques for microwave and thermal infrared remote sensing of the Earth, with a focus on hydrology, water resources management, and vegetation monitoring.

Dr. Kerr was involved with many space missions. He was an EOS Principal Investigator (PI; interdisciplinary investigations) and a PI and Precursor of the use of the SCAT over land. In 1989, he started to work on the interferometric concept applied to passive microwave earth observation and was subsequently the science lead on the MIRAS project for ESA with MMS and OMP. He was also a co-Investigator on IRIS, OSIRIS, and HYDROS for NASA. He was a Science Advisor for MIMR and Co I on AMSR. He is currently a member of the SMAP Science Team. In 1997, he first proposed the natural outcome of the previous MIRAS work with what was to become the SMOS Mission to CNES, proposal which was selected by ESA in 1999 with him as the SMOS mission Lead-Investigator and Chair of the Science Advisory Group. He is also in charge of the SMOS science activities coordination in France. He has organized all the SMOS workshops and was the Guest Editor on three IEEE Special issues and one RSE. He is currently involved in the exploitation of SMOS data in the Cal Val activities and related level 2 soil moisture and level 3 and 4 development and SMOS Aquarius SMAP synergistic uses and on the soil moisture essential climate variable. He is also working on the SMOS-Next SMOS-HR concepts and is involved in both the Aquarius and SMAP Missions. He was nominated for Highly cited Scientist by the Thomson Reuters/Publons, in 2015, 2019, and 2020.

Miguel Colom received the Ph.D. degree in applied mathematics from Universitat de les Illes Balears, Palma, Spain, in 2014.

In 2019, he had the accreditation to supervise research (HDR) with Ecole Normale Superieure Paris-Saclay, Cachan, France, where he is currently a Senior Researcher with Centre Borelli. His research interests include satellite design, image and general signal processing, artificial intelligence, and reproducible research.

Dr. Colom has worked on satellite design (SMOS-HR, IASI-NG) in collaboration with CESBIO and CNES.